Evanescent vortex: Optical subwavelength spanner

Shengtao Mei, Kun Huang, Tianhang Zhang, Muhammad Qasim Mehmood, Hong Liu, Chwee Teck Lim, Jinghua Teng, and Cheng-Wei Qiu

Citation: Appl. Phys. Lett. **109**, 191107 (2016); doi: 10.1063/1.4967745
View online: http://dx.doi.org/10.1063/1.4967745
View Table of Contents: http://aip.scitation.org/toc/apl/109/19
Published by the American Institute of Physics

RIGHTSLINK

Evanescent vortex: Optical subwavelength spanner

Shengtao Mei,[1,2,3,a)] Kun Huang,[3,a)] Tianhang Zhang,[1,2,3,a)] Muhammad Qasim Mehmood,[2,4] Hong Liu,[3] Chwee Teck Lim,[2,5] Jinghua Teng,[3,b)] and Cheng-Wei Qiu[1,2,b)]

[1]*Graduate School for Integrative Sciences and Engineering, Centre for Life Sciences (CeLS), National University of Singapore, #05-01, 28 Medical Drive, Singapore, Singapore 117456*
[2]*Department of Electrical and Computer Engineering, National University of Singapore, 4 Engineering Drive 3, Singapore, Singapore 117583*
[3]*Institute of Materials Research and Engineering Agency for Science Technology and Research (A*STAR), #08-03, 2 Fusionopolis Way, Innovis, Singapore 138634*
[4]*Information Technology University (ITU), 346-B, Ferozepur Rd, Lahore 54600, Pakistan*
[5]*Department of Biomedical Engineering, National University of Singapore, 4 Engineering Drive 3, Singapore 117583*

(Received 14 September 2016; accepted 1 November 2016; published online 9 November 2016)

Conventional optical spanners based on free-space focused vortex beams are very difficult to manipulate subwavelength objects due to the diffraction limit, while optical subwavelength spanners are not explored. Evanescent wave is one potential tool to realize subwavelength trapping. By combining vortex with evanescent field, we find that the evanescent vortex can function as an optical subwavelength spanner. We investigate the factors that will affect the generation/function of this subwavelength spanner, including numerical aperture and topological charge. Further, by calculating the optical force and potential on the illuminated objects, we have demonstrated that the evanescent optical vortex field is able to trap 200 nm polystyrene spherical particles and to rotate them around the ring-shaped field at the same time, making it a subwavelength optical spanner. This mechanism can be used as a tool to study the behaviour of very small objects in physics and biology. *Published by AIP Publishing.* [http://dx.doi.org/10.1063/1.4967745]

Angular momentum of light, either spin angular momentum (SAM) or orbital angular momentum (OAM), could be used to rotate the trapped microscopic objects as an optical spanner.[1–5] However, conventional optical spanners are difficult to trap subwavelength particles due to the diffraction limit. Thus, the size of objects that could be manipulated is limited to micrometre scale.[1,6,7] In recent years, researchers have utilized the evanescent fields and surface plasmons to manipulate sub-micrometre objects.[8–11] The evanescent field breaks the diffraction limit without resorting to special nano-structures, as a result, it shows more convenience and flexibility.[12–14] The proposal of evanescent vortex Bessel beam generated after passing through the photonic crystal merges the evanescent field and vortex beam, which verifies the possibility of trapping and rotating metallic nanoparticles.[14] Nevertheless, how the incident vortex beam influences the properties of evanescent vortex and the corresponding optical force is still not clear, and therefore, it is worthwhile to investigate this phenomenon, particularly, at interfaces, which is more common and widely encountered. In this work, we give a theoretical treatment on the optical properties of evanescent vortex wave produced during total internal reflection (TIR) and its capacity of manipulating the nano-particles on the interface of two common dielectrics. It is verified that evanescent vortex can trap 200-nm-diameter polystyrene spherical particles and simultaneously rotate them around the ring even when the incidental power is as low as 30 mW in a simple traditional optical tweezer setup. This work shows that such optical subwavelength spanner holds the potential of being a promising tool in fundamental physics and biology studies.

We first investigate the TIR of Laguerre-Gaussian (LG) beam. The local skew angle of the Poynting vector of a well-collimated LG beam's phase front is $\tan^{-1}\frac{l\lambda_n}{2\pi R}$ (l: topological charge (TC), λ_n: wavelength in certain materials, R: radius of LG beam's primary ring).[15–19] Two potential strategies of magnifying this skew angle are decreasing the primary radius R of the beam and increasing the l. The size of the beam can be suppressed by a high numerical aperture (NA) objective, whose focusing properties can be approximated by the Debye integral and have been verified experimentally.[4,20–25] The paraxial formulation of the direct ratio relation between l and R is not valid for the non-paraxial case. Therefore, it is urgent to clarify the non-paraxial case, especially under the condition of high l and reflection/transmission upon two media duo to the evanescent phenomena behind it.

We employ circularly polarized LG beams in the following content for the sake of symmetrical energy distribution on any cross section. Considering LG_0^l mode under circular polarization ($\sigma=-1$ for right circular polarization (RCP), and $\sigma=1$ for left circular polarization (LCP)), its electric field near the focal plane can be expressed as:[4]

[a)]S. Mei, K. Huang, and T. Zhang contributed equally to this work.
[b)]Authors to whom correspondence should be addressed. Electronic addresses: jh-teng@imre.a-star.edu.sg and chengwei.qiu@nus.edu.sg

RIGHTSLINK

$$E(r,\phi,z)=\begin{bmatrix}E_{x,\sigma}\\E_{y,\sigma}\\E_{z,\sigma}\end{bmatrix}=-\frac{if}{\lambda_n}\int_0^{\theta_{max}}\int_0^{2\pi}\left(\frac{\sqrt{2}f\sin\theta}{w}\right)^{|l|}e^{-\frac{f^2\sin^2\theta}{w^2}}e^{il\varphi}\sin\theta\times\sqrt{\cos\theta}e^{ik(z\cos\theta+r\sin\theta\cos(\varphi-\phi))}$$
$$\times\begin{bmatrix}\left(\cos^2\varphi\cos\theta+\sin^2\varphi\right)+\sigma i\cos\varphi\sin\varphi(\cos\theta-1)\\\cos\varphi\sin\varphi(\cos\theta-1)+\sigma i\left(\cos^2\varphi+\sin^2\varphi\cos\theta\right)\\\sin\theta e^{i\sigma\varphi}\end{bmatrix}d\varphi d\theta, \quad (1)$$

where $k=\frac{2\pi}{\lambda_n}$ (n is the media refractive index) is the wave number, f is the focal distance, w is the beam waist, φ and θ are shown in Figure 1(a), and $NA=n\sin\theta_{max}$.

In addition, if the beam is focused onto an interface between two different dielectric media (shown in Figure 1(a)), the transmitted and reflected electric field can also be derived with similar expressions, respectively.[20] By imaging the intersecting lines (red oblique lines on the sky-blue plane in Figure 1(a)) between the spiral phase front and the tangent plane (the sky-blue plane shown in Figure 1(a)) at the ring's maximum intensity position, it is straightforward to acquire the two skew angles (α and β) before and after the interface (Figure 1(b)).

These two proposed potential strategies, represent the two factors (NA and l) that are possible to affect the skew angle. Without loss of generality, we assume that Medium I is glass with its refractive index $n_1=1.6$, Medium II is air with its refractive index $n_2=1$, and $\lambda_0=632.8$ nm. Figure 2(a) shows that α increases accompanied with NA at any fixed l, which can be predicted from angular spectrum theory. On the other hand, α increases gradually accompanied with l under the same NA. Although radius of vortex beam is a linearly increasing function of l under the same NA, the value of the skew angle (α) under fixed NA is restricted by $\theta_{\max}$ determined by NA to form an asymptotic tendency. For example, the asymptotic value of α under $NA=1.12$ is about 42° which is slightly smaller than the $\theta_{\max}\approx 44°$. Skew angle of a vortex beam with smaller l can be much smaller compared to bigger l. Vortex beam with larger l presents larger radius at the entrance pupil of the objective lens. As a result, more power is pushed into higher angular spectrum range at the focal plane accordingly, which leads to bigger skew angle. On the transmission side, the skew angle β shows more complex properties as presented in Figure 2(b). For the cases when $NA<1.12$, the skew angle β performs similarly with α, while when $NA=1.12$, β approaches 90° for $l\geq 25$, which means the transmitted wave is already bounded on the interface. Under this circumstance, the propagating optical vortex beam is transformed into evanescent optical vortex wave. When $NA=1.12$ and $l<25$, such incident vortex beam can be decomposed into a set of plane waves, consisting of those with incident angles smaller and larger than the critical angle. Therefore, the skew angle β is smaller than 90° and the transmitted wave is not fully bounded. For remaining cases ($NA=1.28$ and 1.44), β is always 90°, which reveals that the transmitted wave is always evanescent wave. The relation between the two skew angles is roughly but not strictly governed by the Fresnel equation which is derived from the plane wave.

Considering the critical cases discussed above when $NA=1.12$, the propagating vortex beam is gradually transformed into evanescent vortex. To further investigate the influence of l on this vortex beam's TIR, four different sets of [NA, l] ([0.8, 20], [1.12, 5], [1.12, 30], [1.12, 60]) are simulated with the electric field and Poynting vector shown in Figure 3. Figure 3(a) is set as the reference case to show general reflection and transmission before TIR happens. Its top right inset shows that the two dimensional (2-D) Poynting vector always points towards the +z direction, meaning that it is a propagating beam. Its bottom right image, which presents the 3-D Poynting vector on x-y cross-section at $z=100$ nm, is an echo showing the energy flow rotates (P_φ)

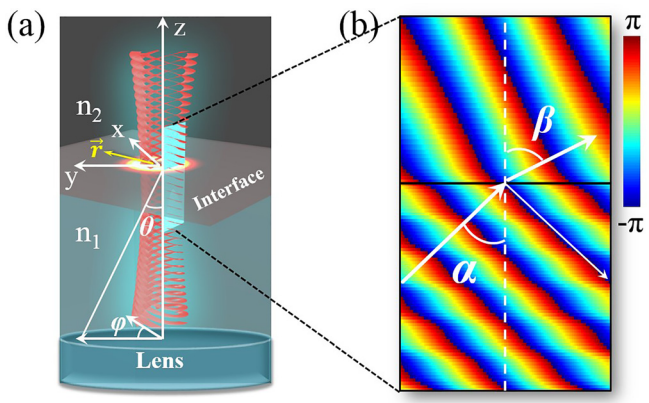

FIG. 1. (a) Illumination of focused LG beam with the focal plane overlapping with the interface between two media. The skew angle can be detected from the tangent plane along the z direction at the primary ring's maximum intensity. (b) Phase front distribution on the tangent plane. α is the skew angle in the dense Medium I, and β is the skew angle in the less dense Medium II.

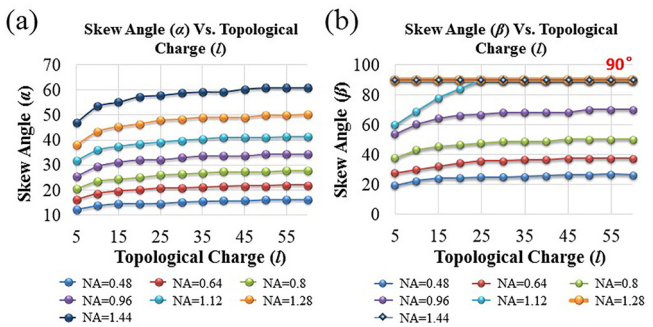

FIG. 2. Skew angles at the incidence and transmission side. Different NA (from 0.48 to 1.44) and l (from 5 to 60) are considered to determine their effects on the skew angles. (a) Skew angles of LG beams at the incident medium are calculated with respect to certain NA and l. (b) Skew angles of LG beams at the transmission medium are calculated with respect to certain NA and l.

RIGHTSLINK

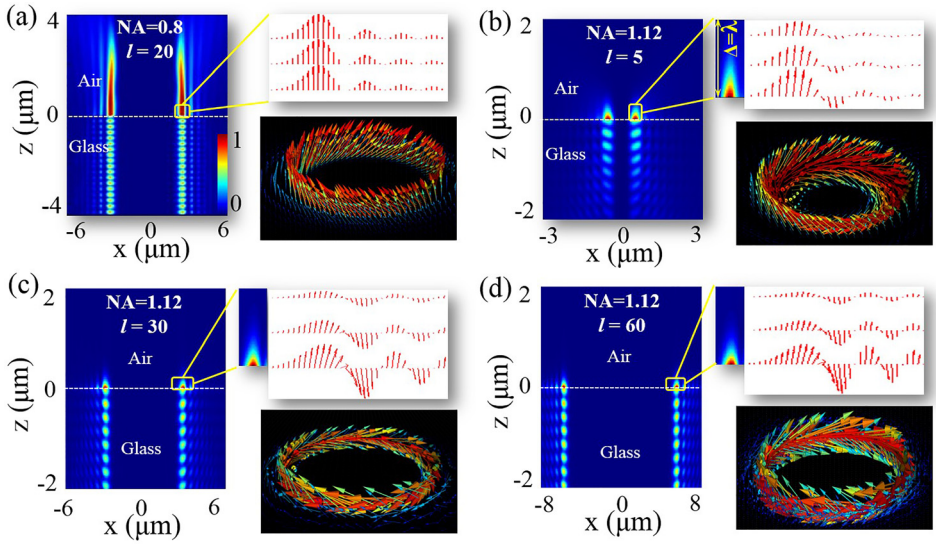

FIG. 3. Reflection and refraction phenomena of different focused LG beams upon the interface between glass ($n_1 = 1.6$) and air ($n_2 = 1$). The bottom right images in (a-d) are the 3-D Poynting vector of the x-y cross-section at $z = 100$ nm. (a) The left image shows the electric intensity near the focal plane (interface) with $NA = 0.8$ and $l = 20$. The inset shows the 2-D Poynting vector at the primary ring above the interface. (b)(c)(d) The left image shows the electric intensity near the focal plane (interface) with $NA = 1.12$ and $l = (5, 30, 60)$. The inset is the magnification of the intensity near the primary ring within one-wavelength distance above the interface. The top right image shows the 2-D Poynting vector at the primary ring above the interface.

and propagates (P_z). While the insets in Figures 3(b)–3(d) are the magnifications of the electric field intensity distribution around the primary ring within one-wavelength distance above the interface. $l = 5$ is a transitional case, from which we can observe that some energy flows back to Medium I and others flow forwards to Medium II, as shown in Figure 3(b). Meanwhile, its 3-D Poynting vector shows bigger P_φ and smaller P_z. This can be considered as partial TIR since only part of the angular spectrum components of the vortex beam meet the condition of TIR. However, by further checking the cases of $l = 30$ and $l = 60$ we can find that almost all of the energy flows back into Medium I. In the 3-D Poynting vector image, P_φ component dominates above the interface which confirms the occurrence of TIR.

It can be also found that the attenuation of the intensity above the interface becomes faster from $l = 5$ to $l = 60$, which can be explained by the increasing of the incident skew angle α. Since β is always real and positive, we lose its imaginary part in Figure 2(b), which carries the information of evanescent wave. However, according to the rough Fresnel relation between α and β, it can be calculated that the imaginary part of β also increases with α. This imaginary part contributes to the increasing absolute value of k_φ above the interface. On the other hand, considering the local linear momentum k from the aspect of momentum conservation, $k^2 = k_\varphi{}^2 + k_z{}^2$ ($k_r \approx 0$ when $z \approx 0$), k_z is imaginary number under TIR, and its absolute value becomes larger according to the electric field's faster attenuation with higher l. Consequently, k_φ also becomes larger. It is worth stressing that such larger k_z (imaginary) and k_φ (real) are realized by increasing the l with fixed NA.

To demonstrate the evanescent vortex as an optical spanner to manipulate subwavelength objects, we calculated and analyzed the optical force on a polystyrene (PS) spherical particle with radius of 100 nm (shown in Figure 4(a)). The field is generated at the interface of flint glass ($n = 1.8$)

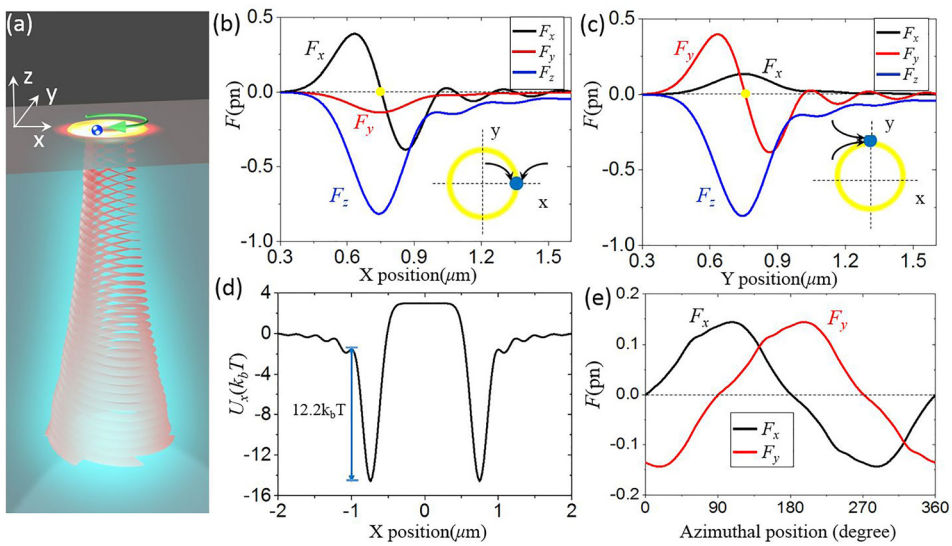

FIG. 4. (a) Schematic of the optical setup: a LG beam with $l = 10$ is focused on the interface of flint glass (lower side) and water (upper side), a PS particle is trapped and rotated by the generated evanescent field. (b) Calculated optical force on the particle in x, y, and z direction at various x positions when the particle is placed $\varphi = 0°$ on the ring (dashed line in the inset). (c) Calculated optical force on the particle in x, y, and z direction at various y positions when the particle is placed $\varphi = 90°$ on the ring (dashed line in the inset). (d) Trapping potential along the x axis, a deep potential well of 12.2 k_bT is found at the primary ring. (e) Calculated optical force on the particle in x and y direction at various trapping positions on the primary ring with different azimuthal angle.

RIGHTSLINK

and water ($n = 1.33$) by focusing a circularly polarized LG beam ($l = 10$) when $NA = 1.53$. The incident power is set as 30 mW and the PS particle is placed at 30 nm above the interface throughout this paper. The total induced time-averaged optical force is calculated by integrating the time averaged Maxwell Stress Tensor (MST) over a closed surface inclosing the particle

$$F = \oint_S \langle \bar{T} \rangle \cdot dS. \tag{2}$$

The time averaged MST is written as

$$\langle \bar{T} \rangle = \frac{1}{2}\mathrm{Re}\left[D \otimes E^* + B \otimes H^* - \frac{1}{2}I(E^* \cdot D + H^* \cdot B)\right], \tag{3}$$

where $\otimes$ represents the dyadic product and I is the identity matrix. The optical forces in x, y, and z directions are calculated at various x positions when the particle is placed $\varphi = 0°$ on the primary ring (inset of Figure 4(b)). In x direction, the particle experiences a restoring force that traps it at the position of $x = 0.77\ \mu$m, where the intensity maximum of primary ring locates. Further along the x direction, other equilibrium positions contributed by the outer rings are also found, but they do not have enough energy to trap the particle, as will be shown later. A pushing force along the y direction could rotate the particle in the clockwise direction. The optical forces versus various y positions are plotted in Figure 4(c) when the particle is placed at $\varphi = 90°$ on the ring. Similar to the $\varphi = 0°$ case, the results suggest that the force could trap and rotate the particle in clockwise direction.

To verify the stability of this optical spanner, we calculated the trapping potential in the radial direction by integrating the optical force:[26] $U(r) = \int_{\infty}^{r} F_r \cdot dr$. At the positon of primary ring, a deep potential well of 12.2 k_bT is found (Figure 4(d)). This potential is larger than the one suggested previously for stable optical trapping (10 k_bT)[27,28] even when the incident power is as low as 30 mW. The other potential wells formed by the outer rings have potentials less than 1% of the primary ring's, thus being insufficient to trap the particle.

We calculated the optical force in x and y direction when the particle is placed on the primary ring (radius of 0.77 μm) at various azimuthal angles. In this case, the trapping force in radial direction $F_r \approx 0$ (refer to Figure S3), and F_x, F_y as a function of the radiation pressure in azimuthal direction F_φ can be written as

$$F_x = F_\varphi \sin\varphi \quad F_y = -F_\varphi \cos\varphi, \tag{4}$$

where φ is the azimuthal angle. F_x and F_y in Figure 4(e) are approximately in cosine and sine shape, implying that F_φ is almost constant along the ring. All in all, we have demonstrated that the evanescent optical vortex field could be used as an optical spanner which can trap nanometre-scale particles in 3-D space and rotate them continuously around its primary ring.

To investigate the beam's effects for the optical manipulation, we calculated the optical forces for beams with different l and NA. The radius of the primary ring increases almost linearly with the l and decreases for higher NA (Figure 5(a)).

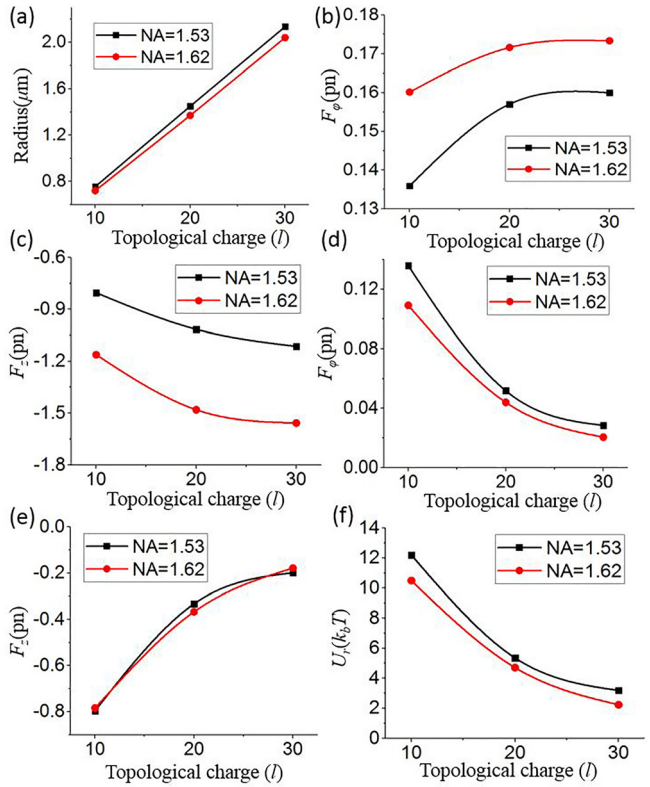

FIG. 5. The way that the properties of the beam affects the properties of the optical spanner. (a) Radius of the primary ring with respect to certain l and NA. (b) Radiation pressure in azimuthal direction and (c) trapping force in z direction with respect to certain l and NA assuming the same local field intensity at the particle centre. (d) Radiation pressure in azimuthal direction and (e) trapping force in z direction and (f) trapping potential of the primary ring with respect to certain l and NA assuming the same input power of 30 mW.

F_φ and F_z could be written as $F_{\varphi,z} \propto I(P, l, NA) \times K(l, NA)$, where I represents the local field intensity at trapping position, K represents the effect of the local field profile, and P is the input power. I and K are both function of l and NA, while I is also proportional to the input power P. At first, to analyse how the field profiles affect those forces, we fix I and calculate the forces for various l and NA. We found that F_φ and F_z both increase for larger l and larger NA (Figures 5(b) and 5(c)). The enhancement of both forces could be explained by the theory we provided in previous paragraphs, namely, when l and NA increase, the screw angle α increases, wave vector in both azimuthal (k_φ: real number) and z (k_z: imaginary number) directions increase their absolute values. Larger real amount of momentum carried by light could be transferred to the particle thus exerts larger force in azimuthal direction. In z direction, the field intensity decays faster for larger $|k_z|$, generating larger gradient force on the particle. Then we fix the input power at 30mW for different l and NA (Figures 5(d)–5(f)). The effect of I on those forces is also considered. When l increases, the area of the primary ring increases making the energy less focused. Although K increases as the screw angle α increases, I drops more dramatically making the forces decrease. When NA increases, two factors have to be considered: (1) the primary ring shrinks causing the energy more focused, (2) the screw angle α increases. (1) and (2) both contribute to larger forces F_φ and F_z. Surprisingly, we found F_φ and F_z remain the same or even decrease for higher NA. We attribute this phenomena to

RIGHTSLINK

a third factor (refer to supplementary material for detailed analysis). This third factor cancels the effects of (1) and (2), making F_φ, F_z, and trapping potential of the primary ring (U_r) remain the same and even decreases for higher *NA*. The effects of these parameters on optical forces are summarized in Table S1 in supplementary material. So far, we have used the theory put forward in previous paragraphs to explain the trends for the forces in our simulations. The simulation results match quite well with the theoretical predictions. In addition, our spanner can be easily realized based on conventional optical spanner setup.

In summary, we demonstrated that the proposed evanescent vortex can function as an optical subwavelength spanner to enrich the manipulations of subwavelength particles. Previous optical spanner works for micron sized particles but fails for smaller ones, while our combination of evanescent field and vortex beam creates the optical subwavelength spanner under the simplest scenario. Such evanescent vortex field can trap and rotate 200 nm polystyrene spherical particles without extra nano-structures. This work stands for the theoretical and simulation demonstration of optical spanner which could trap and rotate subwavelength particles using passive methods. The detailed TIR properties of LG beams together with the subwavelength optical spanner will facilitate and promote the studies of physics and biology applications.

See supplementary material for: (1) For an evanescent field spanner with fixed input power, when *NA* increases, F_φ and F_z remain the same or even decrease. In this situation, we found three factors affecting these forces. The first two factors are illustrated in the main text, while the third one which is the effect of the focal plane is described in this part including Figure S1. (2) At fixed input power, when l and *NA* changes, there are a few factors affecting the forces F_φ and F_z. These factors are summarized in this part including Table S1. (3) The evanescent field spanner also generates force in z direction to trap the particles to the surface. The trapping force and potential in z direction including Figure S2 is described in this part. (4) The evanescent vortex is not a perfect ring. The fluctuation in trapping radius and azimuthal force including Figure S3 is illustrated in this part.

This research was supported by the National Research Foundation, Prime Minister's Office, Singapore under its Competitive Research Programme (CRP Award No. NRF-CRP10-2012-04). The work was also partially supported by Agency for Science, Technology and Research (A*STAR) under Grant Nos. 152-148-0031 and 152-700-0014.

[1]H. He, M. E. Friese, N. R. Heckenberg, and H. Rubinsztein-Dunlop, Phys. Rev. Lett. **75**, 826 (1995).
[2]N. B. Simpson, K. Dholakia, L. Allen, and M. J. Padgett, Opt. Lett. **22**, 52 (1997).
[3]V. Garces-Chavez, D. McGloin, M. J. Padgett, W. Dultz, H. Schmitzer, and K. Dholakia, Phys. Rev. Lett. **91**, 093602 (2003).
[4]Y. Zhao, J. S. Edgar, G. D. Jeffries, D. McGloin, and D. T. Chiu, Phys. Rev. Lett. **99**, 073901 (2007).
[5]B. J. Black and S. K. Mohanty, Opt. Lett. **37**, 5030 (2012).
[6]D. G. Grier, Nature **424**, 810 (2003).
[7]A. M. Yao and M. J. Padgett, Adv. Opt. Photonics **3**, 161 (2011).
[8]O. M. Marago, P. H. Jones, P. G. Gucciardi, G. Volpe, and A. C. Ferrari, Nat. Nanotechnol. **8**, 807 (2013).
[9]A. N. Grigorenko, N. W. Roberts, M. R. Dickinson, and Y. Zhang, Nat. Photonics **2**, 365 (2008).
[10]D. Woolf, M. A. Kats, and F. Capasso, Opt. Lett. **39**, 517 (2014).
[11]X. Xu, C. Cheng, H. Xin, H. Lei, and B. Li, Sci. Rep. **4**, 3989 (2014).
[12]H. Xin and B. Li, Opt. Express **19**, 13285 (2011).
[13]H. Xin, C. Cheng, and B. Li, Nanoscale **5**, 6720 (2013).
[14]G. Rui, X. Wang, and Y. Cui, Opt. Express **23**, 25707 (2015).
[15]L. Allen, M. W. Beijersbergen, R. J. Spreeuw, and J. P. Woerdman, Phys. Rev. A **45**, 8185 (1992).
[16]M. W. Beijersbergen, R. P. C. Coerwinkel, M. Kristensen, and J. P. Woerdman, Opt. Commun. **112**, 321 (1994).
[17]J. Leach, S. Keen, M. J. Padgett, C. Saunter, and G. D. Love, Opt. Express **14**, 11919 (2006).
[18]G. C. G. Berkhout, M. P. J. Lavery, J. Courtial, M. W. Beijersbergen, and M. J. Padgett, Phys. Rev. Lett. **105**, 153601 (2010).
[19]N. Yu, P. Genevet, M. A. Kats, F. Aieta, J.-P. Tetienne, F. Capasso, and Z. Gaburro, Science **334**, 333 (2011).
[20]D. Biss and T. Brown, Opt. Express **9**, 490 (2001).
[21]D. Ganic, X. Gan, and M. Gu, Opt. Express **11**, 2747 (2003).
[22]Q. Zhan, Opt. Lett. **31**, 1726 (2006).
[23]H. Wang, L. Shi, B. Lukyanchuk, C. Sheppard, and C. T. Chong, Nat. Photonics **2**, 501 (2008).
[24]K. Huang, P. Shi, X. L. Kang, X. Zhang, and Y. P. Li, Opt. Lett. **35**, 965 (2010).
[25]M. Gu, *Advanced Optical Imaging Theory*, Springer Series in Optical Sciences (Springer, Berlin; New York, 2000), p. 75.
[26]L. Novotny, R. X. Bian, and X. S. Xie, Phys. Rev. Lett. **79**, 645 (1997).
[27]A. Ashkin, J. M. Dziedzic, J. E. Bjorkholm, and S. Chu, Opt. Lett. **11**, 288 (1986).
[28]M. L. Juan, M. Righini, and R. Quidant, Nat. Photonics **5**, 349 (2011).

RIGHTSLINK